Wind Tunnel Aerodynamic Tests of Six Airfoils for Use on Small Wind Turbines

Michael S. Selig*
e-mail: m-selig@uiuc.edu

Bryan D. McGranahan†
e-mail: mcgranah@uiuc.edu

Department of Aerospace Engineering,
University of Illinois at Urbana–Champaign,
Urbana, IL 61801

This paper presents detailed wind tunnel tests data taken on six airfoils having application to small wind turbines. In particular, lift, drag and moment measurements were taken at Reynolds numbers of 100,000, 200,000, 350,000 and 500,000 for both clean and rough conditions. In some cases, data were also taken at a Reynolds number of 150,000. The airfoils included the E387, FX 63-137, S822, S834, SD2030, and SH3055. Prior to carrying out the tests, wind tunnel flow quality measurements were taken to document the low Reynolds number test environment. Oil flow visualization data and performance data taken on the E387 compare favorably with measurements taken at NASA Langley in the Low Turbulence Pressure Tunnel. Highlights of the performance characteristics of the other five airfoils are presented. [DOI: 10.1115/1.1793208]

Introduction

This paper documents the aerodynamic characteristics of six airfoils, which were also examined in a companion study dealing with their aeroacoustic properties [1]. These projects together were motivated by two intersecting factors. First, the U.S. Department of Energy, National Renewable Energy Laboratory (NREL), has initiated research into the aeroacoustics of wind turbines, which is an important design consideration when a potentially valuable wind resource and a population center coincide. Such an event—the confluence of wind technology and people—is increasingly probable as wind turbines become more efficient and better able to exploit lower wind speed sites, which are often found near U.S. load centers. Improving our understanding of the aeroacoustics will help designers exploit advances in noise mitagation design strategies. It is anticipated that having a reliable and self-consistent airfoil performance data set may be helpful in validating aeroacoustics prediction codes in support of such design activities. Second, small stand-alone wind turbines operating in close proximity to residential areas posed a noise concern. Given that the aerodynamic efficiency increases with the tip speed and hence wind turbine noise, advances in the development of small wind turbines can be envisioned using a suite of computational tools capable of predicting both the aeroacoustic characteristics and aerodynamic performance. Thus, an aerodynamic data set of representative wind turbines airfoils should help pave the way toward the development of the necessary design methodologies needed by the small wind turbine industry seeking to improve efficiency as well as acceptability.

Wind Tunnel Facility and Models

All experiments were conducted in the University of Illinois at Urbana–Champaign (UIUC) subsonic wind tunnel (Fig. 1), which has a nominal test section that is 2.81-ft high and 4-ft wide. The low Reynolds number setup used in these tests and depicted in Fig. 2 has been previously documented [2,3]. Two 6-ft long Plexiglas™ splitter plates were inserted 2.8 ft apart into the test section to isolate the airfoil models from both the support hardware and the tunnel sidewall boundary layers. For clarity, these splittler plates are not shown in in Fig. 2, however a photograph of these details can found in Ref. [4]. The 1-ft chord airfoil models were inserted horizontally between the splitter plates with nominal gaps of 0.040–0.080 in. between the end of the airfoil model and the splitter plates. Performance data were taken at Reynolds numbers of 100,000, 200,000, 350,000 and 500,000. In some cases, data were also taken at a Reynolds number of 150,000. The lift was measured using a strain gauge load cell, and the drag was determined using the momentum deficit method [2]. To account for spanwise drag variations at low Reynolds numbers [5], the drag was obtained from an average of eight equidistant wake surveys over the center of the model so that a 10.5-in. wide span was covered. The overall uncertainty in both the lift and drag measurements was estimated at 1.5% [2,3]. All lift and drag measurements were corrected for wind tunnel interference and validated with data from the NASA Langley Low Turbulence Pressure Tunnel [2,5,6].

The wind tunnel tests included a broad variety of airfoils that are summarized in Table 1. It should be mentioned that later suffixes are added to the airfoil names (e.g. ''(E)'') and used in the captions to indicate the wind-tunnel model versions of those particular airfoils. For instance, the E387 (E) case is the fifth model of the E387 airfoil in the UIUC collection.

The airfoil models were shaped in a computer numerically controlled milling machine out of RenShape high-density foam, structurally reinforced, fiberglassed, then sanded and painted. A coordinate-measuring machine was used to digitize the models [3]. The differences between the nominal and measured coordinates were calculated, allowing the computation of an average accuracy for each model (mean of the differences). For the airfoils used in the current study, the differences between the nominal and measured coordinates are indicated in Fig. 3 underneath the airfoil names.

Tunnel Flow Quality and Validation

As has been well documented, low Reynolds number airfoil flows are highly sensitive to the tunnel flow quality. Consequently, tunnel flow quality measurements were taken and documented as described below.

Turbulence Intensity Measurements. The turbulence intensity was measured using hot-wire anemometry. The hot-wire system was a TSI Incorporated IFA 100 anemometer in conjunction with a TSI Model 1210-T1.5 hot-wire probe. The probe makes use of a 1.5-μm platinum-coated tungsten wire. The probe was

---

Fig. 1 UIUC low-speed subsonic wind tunnel

Fig. 3 Airfoils tested and their corresponding average error in inches for the 12-in. chord models presented in this study
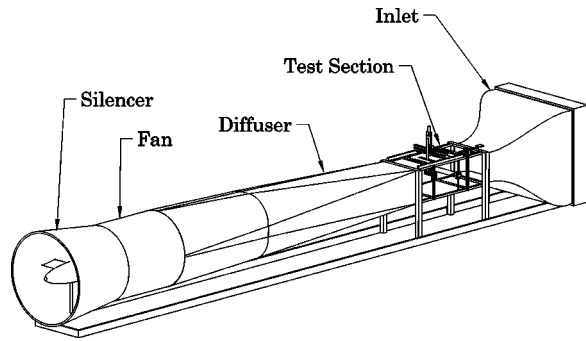
mounted in the tunnel end-flow orientation with the wire perpendicular to the tunnel floor in order to measure the axial turbulence intensity. A PC equipped with a data acquisition card was used to log the signal from the anemometer. A HP 35665A Dynamic Signal Analyzer, which performed a FFT (fast Fourier transform) analysis, was employed to allow the turbulence spectrum to be monitored over a broad range of frequencies. More details of the method are given in Ref. [4].

The turbulence intensity was calculated from data using a total of 50,000 samples with a sample frequency of 10,000 Hz. Figure 4 shows the resulting turbulence levels for both the tunnel empty case and with the full measurement apparatus installed. In general these levels are considered to be sufficiently low for taking low Reynolds number airfoil measurements.

Dynamic Pressure Surveys. The variation in the dynamic pressure in the test section of the UIUC low-speed subsonic wind tunnel was obtained by comparing the dynamic pressure at a pitot-static probe mounted near the entrance of the splitter plates with that measured by a downstream probe. The upstream probe was located at the centerline of the tunnel in the spanwise direction
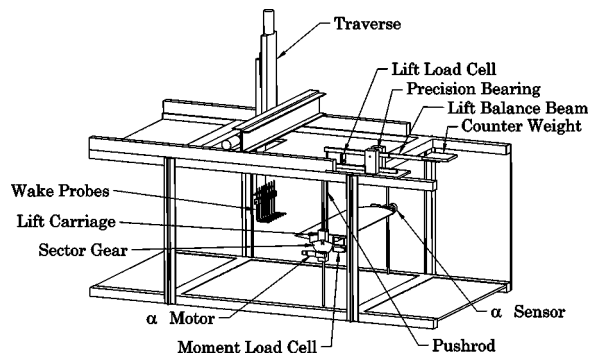

Fig. 2 Experimental setup (Plexiglas splitter plates and traverse enclosure box not shown for clarity)

Table 1 Airfoils tested

| Airfoil	Relevance/usage
E387	Benchmark Eppler airfoil tested in NASA Langley LTPT
FX 63-137	Aeromag Lakota, Southwest Windpower H-40, H-80 and candidate for next-generation small wind turbine
S822	AOC/Windlite, Havatex 2000 and candidate for next-generation small wind turbine, patented by DOE NREL
S834	New low-noise, low-Re airfoil and candidate for next-generation small wind turbine, patent pending by DOE NREL
SD2030	Southwest Windpower Air 403 and Air X turbines
SH3055	Bergey Windpower Excel turbine
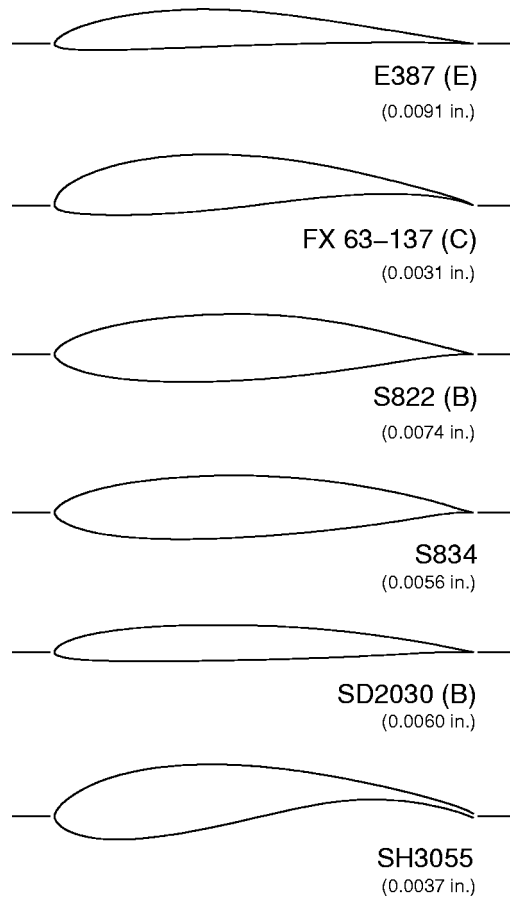
$(X=0\text{ in.})$, 0.97 ft below the centerline of the tunnel in the vertical direction $(Y=-11.66\text{ in.})$, and 1.323 ft upstream of the quarter-chord location of the airfoil model when mounted in the test section. The downstream probe was traversed in the X-Y plane perpendicular to the freestream and coincident with the quarter chord. Measurements were made both with the test section empty and with the test apparatus installed.

The measurement plane extended from 5.5 in. above the tunnel centerline to 14.5 in. below in the vertical direction Y, and from 10.5 in. to the left of the tunnel centerline to 10.5 in. to the right in the horizontal direction X. A grid spacing of 1 in. was used for the measurements, resulting in a total of 462 measurement points for each case tested.

A total of three differential-pressure transducers were used for the measurements. One transducer measured the upstream dynamic pressure Q_u by measuring the pressure difference across the total pressure and static pressure ports of a pitot-static probe. A second pressure transducer was configured to measure the difference between the upstream and downstream total pressure ΔP_0. A third transducer was configured to measure the difference between the upstream and downstream static pressure Δp. The change in dynamic pressure ΔQ is just $\Delta P_0 - \Delta p$. Thus, the local dynamic pressure at each point is therefore

$$Q = Q_u + \Delta Q = Q_u + \Delta P_0 - \Delta p \qquad (1)$$

For each Reynolds number tested, the tunnel speed was set using the upstream probe as the reference. Differences in temperature and ambient pressure were accounted for. The percent difference at each point was calculated according to
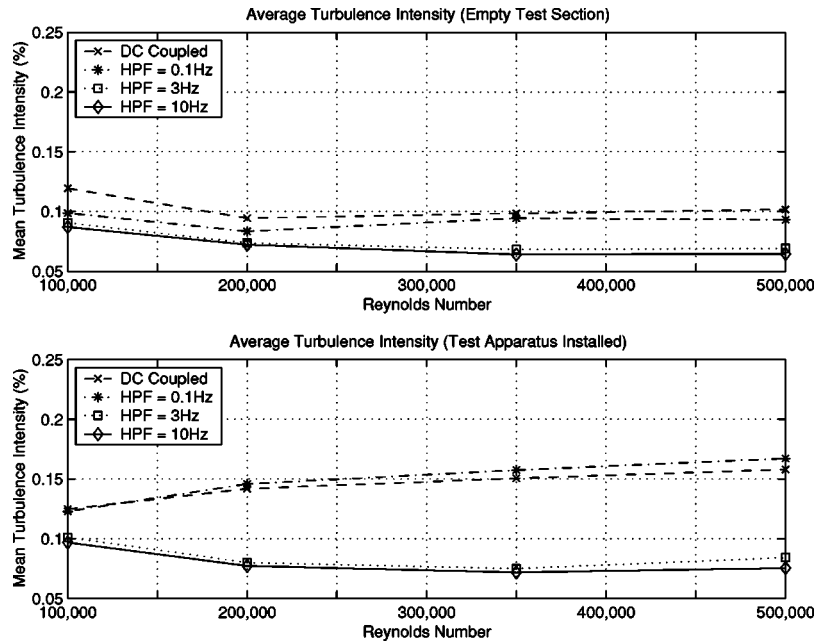
Fig. 4 Turbulence intensity at tunnel centerline, empty test section and with rig in place

$$\Delta Q(\%) = \frac{Q - Q_u}{Q_u} \times 100\% \tag{2}$$

Figure 5 shows contours of ΔQ for various Reynolds numbers plotted against its X and Y location for the case with the test rig installed. Several observations can be made. There is a slight increase in the flow speed in going downstream. It is likely that the velocity measured at the location of the model is higher than the upstream velocity because of the growth of the boundary layer along the splitter plates, ceiling and floor as well as the blockage that occurs between the splitter plates and the tunnel sidewalls. This percentage increase in the flow speed grows larger as the
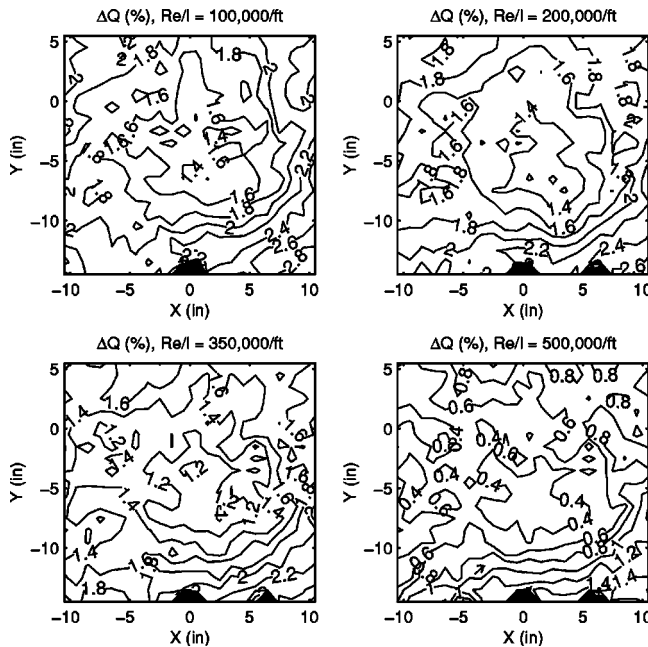

Fig. 5 Dynamic pressure variation across test section with the test rig installed

Reynolds number is reduced, which is consistent with the thicker wall boundary layers at the lower Reynolds numbers. This rise in the velocity is accounted for in the airfoil-performance data-reduction procedure. Second, it is observed that over the region where the model is located, the net change in flow speed is relatively small. For instance, Fig. 5 shows that at Re/l=200,000/ft the increase in the flow speed ranges from approximately 1.4% to 1.8%, which is a relative difference of ±0.2% in the working range of the test section. As stated in Ref. [7], it is desirable to have the variation in dynamic pressure in the working range of the test section be less than 0.5% from the mean, i.e., ±0.5%. The results show that the flow is well within the "rule of thumb." A third observation, is the existence of a slight asymmetry in the flow, noticeable mainly in the $+X:-Y$ quadrant (bottom right corner in Fig. 5). The asymmetry is present with the tunnel empty and with the test rig in place, hence it is unrelated to the test rig. Moreover, the lines of constant Q are parallel to the tunnel floor at $X=0$ (centerline), so the effect is negligible with respect to the performance-measurement quantities in the center region of the test section.

Flow Angularity Surveys. Just as it is important to have uniform flow velocity in the wind-tunnel test section, it is equally important to have the flow parallel to the axial direction [7]. For the most part, pitot-static probes are insensitive to flow angles in the range ±12 deg, so a large flow angle is required to introduce an error in the dynamic pressure measurements. Similarly, large flow angles are required to introduce errors into total head measurements. Apart from pressure measurements, a small change in pitch angle, however, contributes to a change in the effective angle of attack of the airfoil model and thereby such an error can skew the lift and drag measurements when they are plotted versus the angle of attack.

The flow angularity in the test section of the UIUC low-speed subsonic wind tunnel was measured using an Aeroprobe Corporation Model S7TC317 seven-hole probe shown in Fig. 6. The probe has a total-head port located at the center, and six chamfered ports equally spaced circumferentially around the center. The probe was mounted in the wind tunnel on a special two-beam sting attached to the computer-controlled LinTech traverse. The flow measure-
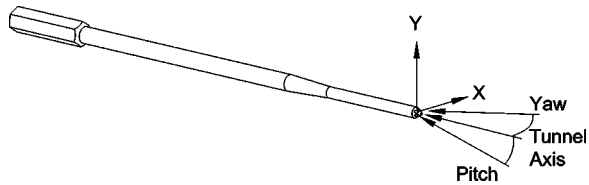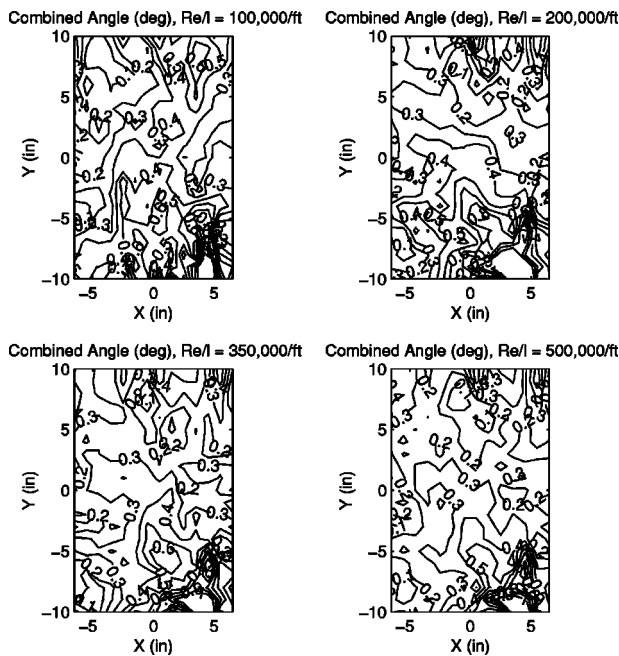
Fig. 6 Illustration of the seven-hole probe used for flow angle measurements
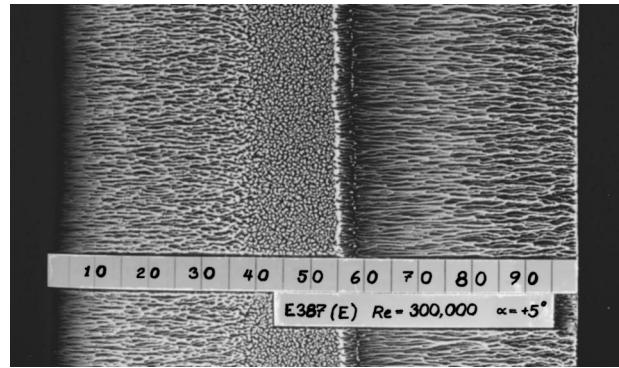
ments were all taken with the test rig installed in the wind-tunnel test section, without the model. A more detailed description of the use of the 7-hole probe is found in Ref. [8].

The seven-hole probe was traversed in a plane perpendicular to the freestream flow over the range from $X = \pm 6.5$ in. to $Y = \pm 10$ in. The traverse was not extended to the edges of the test section due to equipment limitations. Traversing this central core was acceptable because one would expect to find the largest flow angle variation in the center of the test section rather than along the walls where, at a minimum, the flow is parallel to the wall (yaw or pitch is thereby zero). A grid spacing of 1 in. was used, resulting in a grid of 252 sample locations for each case tested. The seven-hole probe tip was located approximately 1.5 chord lengths behind the quarter chord of the airfoil model. To set the tunnel speed, one pitot-static probe was located at $X = 0$ in., $Y = -11.66$ in. For redundancy an additional probe was located at $X = 5$ in., $Y = -11.66$ in. Both pitot-static probes were mounted at the same streamwise location, 1.323 ft upstream of the location of the quarter chord of the airfoil model.

The results shown in Fig. 7 indicate that the total flow angle (pitch and yaw combined) were smallest at Re=500,000, becoming more pronounced at lower Reynolds numbers. The pitch angle measurement (not shown) was generally between 0 and 0.2 deg (± 0.1 deg) across the working region of the test section where the airfoil model is located. According to Ref. [8], a flow angle variation of ± 0.2 deg is acceptable, but ± 0.1 deg or better is the preferred. The current measurements meet this latter desired level of flow quality.


Fig. 8 Representative upper-surface oil flow visualization on the E387 (E), Re=300,000, α=5 deg. (Flow is from left to right and the tape indicates the chordwise distance from the airfoil leading edge.)

Airfoil Data Validation

In this section, data taken on the E387 is compared with results from NASA Langley in the Low-Turbulence Pressure Tunnel (NASA LTPT) [9,6]. Four types of data are compared: surface oil flow visualization, lift data, moment data and drag polars. In this order, these data are presented and discussed below.

Surface Oil Flow Visualization. The surface oil flow visualization technique made use of a fluorescent pigment (Kent-Moore 28431-1) suspended in a light, household-grade mineral oil that was sprayed onto the surface of the model using a Paasche Model VL double-action airbrush. The model was then subjected to 20–45 min of continuous wind-tunnel run time at a fixed Reynolds number and angle of attack. During this period, the oil moved in the direction of the local flow velocity at a rate dependent on the balance of forces dictated by the boundary-layer skin friction coefficient C_f and surface tension of the oil. As a result, regions of the flow could be identified and compared with the NASA Langley Low-Turbulence Pressure Tunnel (LTPT) data [9,6].

Figure 8 shows a photograph of the surface oil flow pattern made visible under fluorescent light. Figure 9 conceptually illustrates the connection between the salient surface oil flow features

Fig. 7 Combined pitch and yaw angle across test section with the rig installed
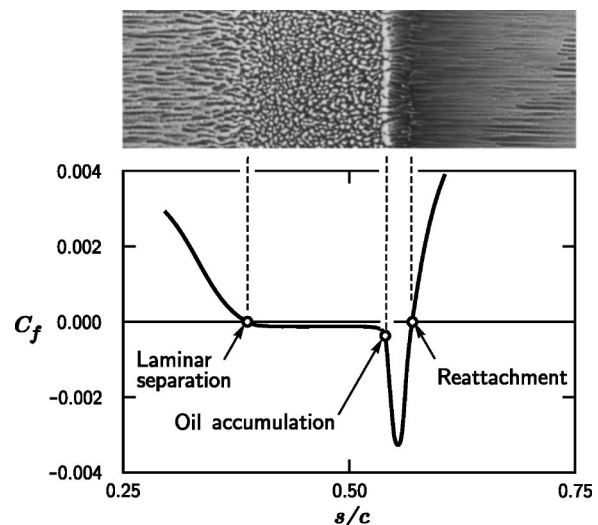
Fig. 9 Conceptual illustration of the relationship between the surface oil flow features and skin friction distribution in the region of a laminar separation bubble plotted against the airfoil arc length coordinate s/c

and the skin friction distribution. Note that the skin friction distribution, though conceptual, is consistent with the results of many computational studies [10–15]. The authors believe that the unique shape of the C_f distribution, in particular the strong negative C_f spike, has yet to be experimentally verified (as no experimental data could be found); however, the oil flow patterns observed seem to confirm the validity of the negative C_f spike concept.

Several important flow features can be identified and related to the underlying skin friction and surface tension forces. In Fig. 8, laminar flow is seen to exist from the leading edge to approximately $0.40c$. The oil streaks are characteristically smooth in this region until laminar separation occurs, which is identified in Fig. 9 as the point where $C_f = 0$. (Note again that the flow shown in Fig. 9 is conceptual, and it is not intended to match Fig. 8 in detail.) Downstream of the point of laminar separation, the original air-brushed "orange-peel" texture that existed prior to running the tunnel still exists, indicating that the flow is stagnant in this region. This stagnant flow is consistent with the known behavior of flow in the interior of a laminar separation bubble. As sketched, the C_f magnitude in this region is quite small due to the low flow speed and negative in sign due to reverse flow at the surface.

In the presence of a laminar separation bubble, transition takes place in the free shear layer above the surface of the airfoil. Downstream of this point, reattachment occurs in a process that is known to be unsteady as vortices are periodically generated and impinge on the airfoil surface [15,16]. These unsteady vortices colliding with the surface lead to a relatively high shear stress that tends to scour away the oil at the mean reattachment point, pushing oil upstream or downstream of the reattachment point. As seen in Fig. 9, the reattachment line is less distinct because the bulk of the oil has been pushed away, revealing the underlying black airfoil surface. In Fig. 8, the tunnel run time was long enough that the reattachment line at $0.58c$ is even harder to see than in Fig. 9. In the original high-resolution color photographs that were archived, this feature is clear and easily quantifiable.

Downstream of reattachment the boundary layer is turbulent. The high skin friction in this area relative to the laminar boundary layer upstream tends to clear away more oil, again making the black surface downstream more visible than in the upstream region.

The remaining visible feature of the flow is a line where the oil tends to pool, termed here the "oil accumulation line." This intrinsic feature of the oil flow has no direct connection to laminar flow, reverse flow in the bubble, or the ensuing turbulent flow downstream. However, it does indicate a relatively important feature of the flow with regard to the nature of the skin friction in the vicinity of reattachment. The negative C_f spike shown in predictions and sketched conceptually in Fig. 9 is most likely responsible for generating the oil accumulation line. Assuming that this is the case, the fluctuating high skin friction that is generated over the unsteady reattachment zone will tend to push the oil upstream ahead of the mean reattachment point. At some location on the airfoil, however, the oil moving upstream will experience a balance of forces between the rapidly weakening skin friction force and that of the surface tension and oil adhesion that is retarding its motion. At the location where these two forces balance, the oil accumulates into a line that becomes the most distinguishable feature of the oil flow. Consequently, it is speculated that this flow feature is sometimes mislabeled as "reattachment" as will be discussed below.

Figures 10 and 11 show the previously described flow features compared with data obtained at the NASA Langley LTPT. In the low drag range between -2 deg and 7 deg angle of attack, the agreement in the laminar separation line between the NASA LTPT and UIUC data sets is mostly within $0.01c$ to $0.02c$, which is very near the uncertainty of the method. As previously discussed, the next feature to appear is the oil accumulation line. The UIUC oil accumulation line agrees fairly well with the "reattachment" line identified in the NASA experiment. It is believed, however, that based on the previous reasoning, this label given in the original Ref. [7] is a misnomer. Had the UIUC tests been performed for a
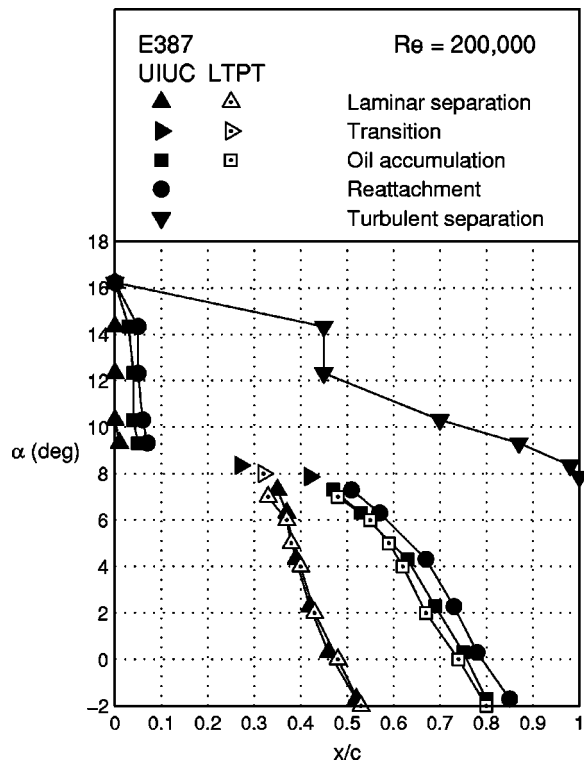

Fig. 10 Comparison of major E387 (E) upper-surface flow features between UIUC and LTPT for Re=200,000
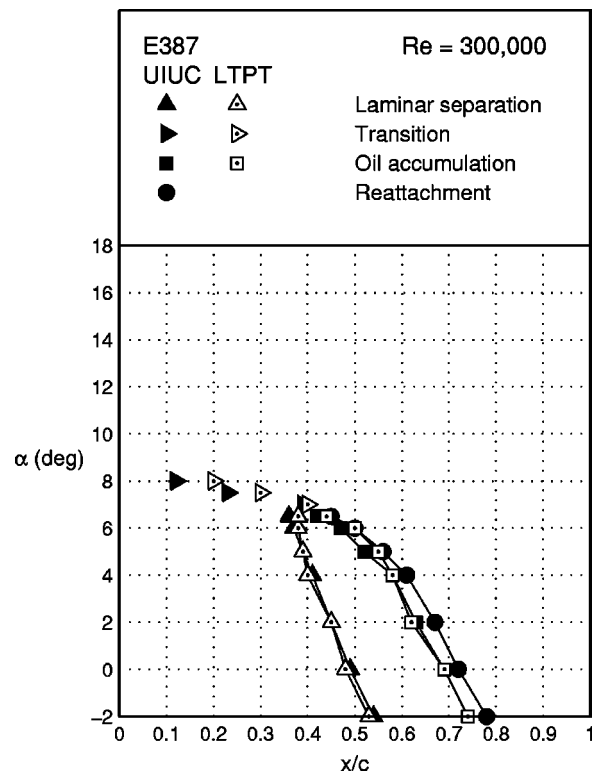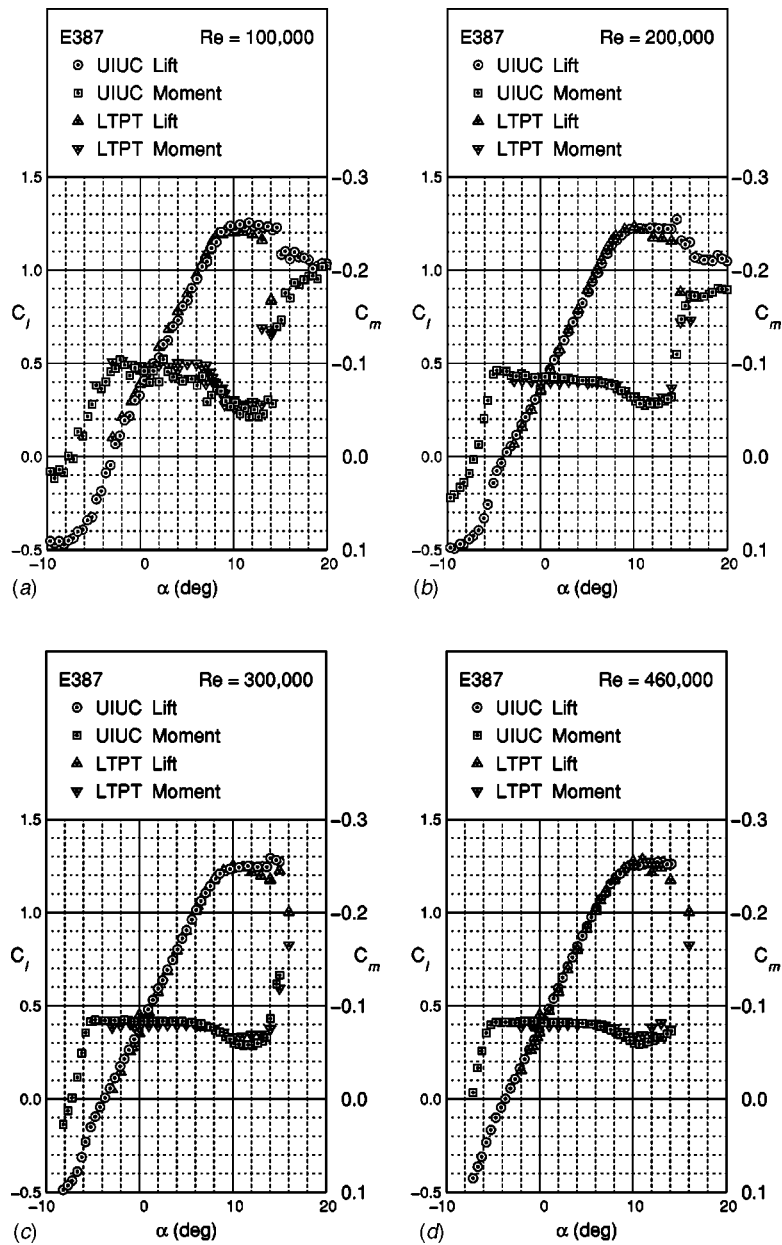

Fig. 11 Comparison of major E387 (E) upper-surface flow features between UIUC and LTPT for Re=300,000

Fig. 12 Comparison between UIUC and LTPT E387 lift and moment coefficient data for Re=100,000, 200,000, 300,000, and 460,000

longer duration, the reattachment zone would have been scoured clean with no distinguishing feature, leaving only the oil accumulation line to be labeled as the "reattachment line," knowing that one must exist. Hence, it is speculated here and in prior UIUC work (Ref. [3]) that such a scenario took place in the NASA study, i.e., the oil-accumulation line was misinterpreted as the reattachment line.

Guided by this working assumption, the two results again are in good agreement. It must be stated, however, that the oil accumulation line might change slightly from one facility to the next since it is dictated by a force balance that depends on the skin friction forces of the boundary layer relative to the adhesion forces of the particular oil used. The predictions, however, show that the negative C_f region has a sharp upstream edge, which is most likely where the oil accumulates regardless of the surface

tension characteristics. Differences in the oil accumulation line due to differences in the type of oil used are therefore believed to be small. The good comparisons between UIUC and Langley data tend to support this assumption.

Moving further downstream, the UIUC reattachment data are plotted, but unfortunately no direct comparison can be made because of the ambiguity with respect to the reattachment data reported in the NASA study. However, close inspection of the data suggests that at a Reynolds number of 300,000 and between 5 deg and 7 deg angle of attack, the LTPT line merges with the UIUC reattachment line. Perhaps in this case, the measurements at Langley were indeed the reattachment points.

The conclusion to be drawn from this comparison of the oil flow visualization results is that the two facilities produce airfoil flows that are in close agreement. Moreover, if the arguments
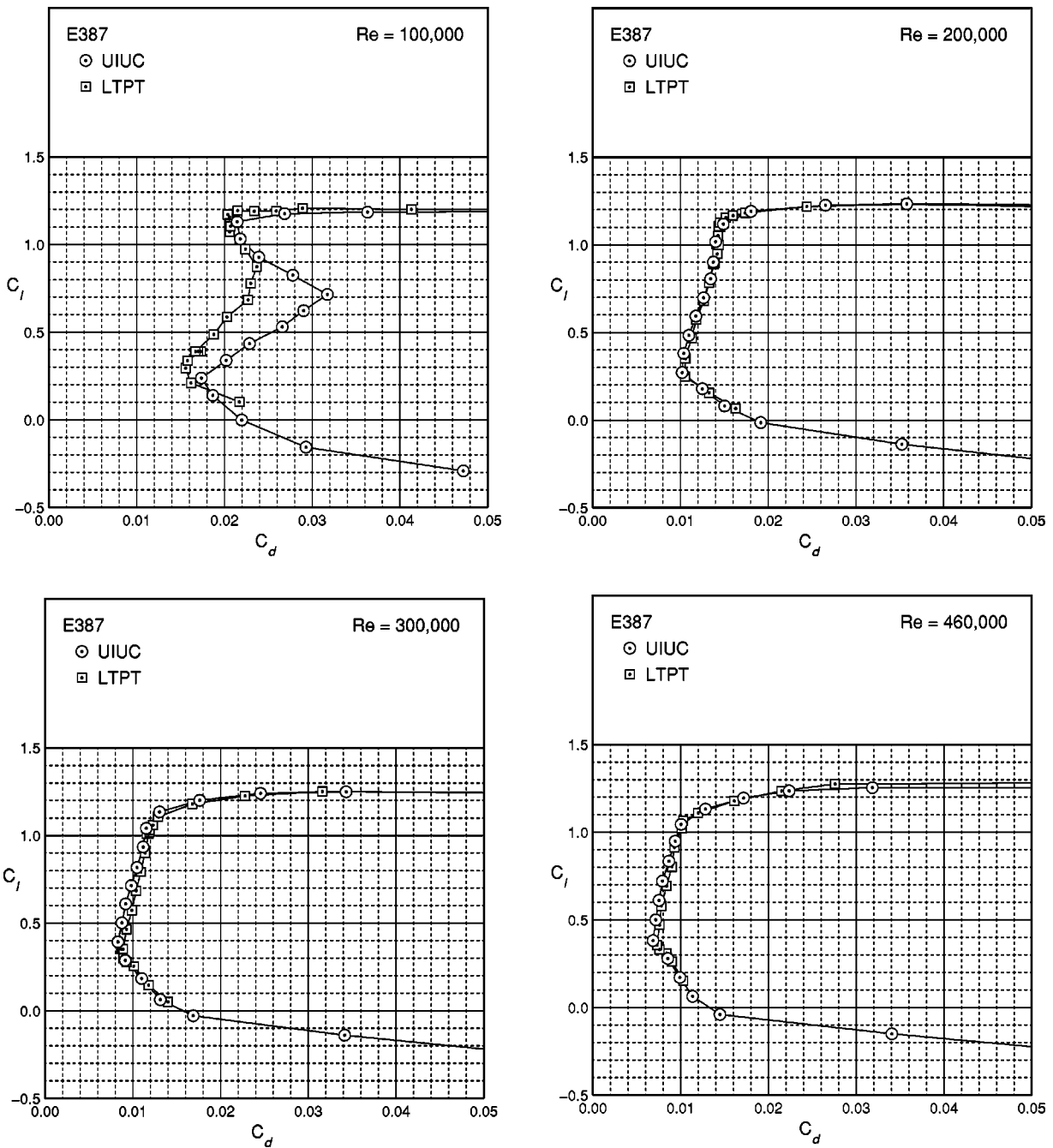
Fig. 13 Comparison between UIUC and LTPT E387 drag coefficient data for Re=100,000, 200,000, 300,000, and 460,000

regarding the oil accumulation line are correct, then the agreement can be considered excellent and within the uncertainty of the measurements.

Lift Data. Lift and moment data comparisons between the UIUC and LTPT data are shown in Fig. 12. Discrepancies can be seen for a Reynolds number of 100,000 as well as in the stalled regime for all Reynolds numbers. For Re=100,000 differences are most likely attributable to measurement accuracy. In stall for $\alpha > 12$ deg, taking the Langley data as the benchmark, the UIUC data differs most likely as result of three-dimensional end effects. Nevertheless, the results show good agreement over the normal unstalled operating range, and this agreement improves with higher Reynolds number.

Drag Data. Figure 13 shows a comparison between UIUC and NASA LTPT drag data for the Reynolds numbers of 100,000, 200,000, 300,000 and 460,000. For a Reynolds number of 200,000 and 300,000, the oil flow results were in close agreement, as were the lift data. Taken together, these results suggest that the drag data should likewise be in good agreement. Indeed, for Re =200,000, the agreement is quite acceptable. However, for Re =300,000 the agreement is not as good. For Re=460,000, the agreement improves, while for Re=100,000, there is less agreement. When these cases are studied in more detail, it is seen that the edges of the drag polar are in quite close agreement for each case, with the Re=100,000 perhaps being the exception.

There can be many reasons for the observed discrepancies, not

the least of which is the fact that at low Reynolds numbers the drag data, when determined from downstream wake measurements, varies along the span—the further downstream, the more variation. The current measurements were taken 1.25 chord lengths downstream of the trailing edge, while those in the NASA study were taken 1.5 chord lengths downstream. Because of this spanwise variation in drag, ideally many wake profile measurements should be taken along the span and the resulting drag coefficients summed and averaged. This approach of performing multiple wake surveys was taken in the current study (as mentioned previously eight wake surveys were taken), but in the NASA study, the full polar data that were reported were acquired by rake data taken at only one station. However, some limited spanwise data was taken in the NASA study, and the degree of spanwise variation observed is quite similar to that found in the current study [4]. Consequently, the discrepancies, in part, must be related to the variation in drag, and had data been taken at many stations in the NASA study, it is likely that better agreement would be observed.

For the Reynolds number of 100,000, which was not critical to the current investigation, the discrepancies are larger. This result cannot be attributed solely to spanwise drag variation. Figure 13 shows that at a $C_l = 0.7$ and Re=100,000, the eight C_d data points obtained from the eight wake measurements fall nearly one on top of the other. Therefore, the spanwise variation in drag is small on a percentage basis, and a similar variation in C_d for this particular case was seen in the NASA data. Consequently, for Re=100,000 the cause for the bulk of the difference in the drag measurements must be something other than spanwise drag variation.

When sources of error were being considered to explain the discrepancies, several factors were ruled out in light of the excellent agreement in surface oil flow visualization and lift and moment data. Of those that remained, no sources of uncertainty in the current data lingered after investigation. Thus, the reason for the disagreement in the drag data for the Reynolds number of 100,000 remains unexplained. It is recognized that the source of this discrepancy might likely relate to some of the discrepancies for the higher Reynolds number cases as well. Nevertheless, the agreement overall is good, especially in light of past historical comparisons of low Reynolds number airfoil data, which vary widely [2,17].

In summary, this section has made several important points that should instill confidence in the data presented in this paper. First, it was shown that surface oil flow data obtained on the E387 airfoil exhibited excellent agreement with NASA LTPT data for Re=200,000 and 300,000. Second, current lift data was shown to have good agreement with LTPT data for all Reynolds numbers up to stall, after which point three-dimensional end effects and unsteady aerodynamics produced slight discrepancies. Third, the pitching moment data was shown to agree well with LTPT data over a broad range of angles of attack. Lastly, in support of the three previous conclusions, the drag data showed good agreement, with some discrepancies yet to be fully explained.

Results and Discussion

In the remainder of this paper, the performance characteristics of each of the airfoils are discussed in detail. Rather than organizing this discussion by commenting on broad categories of various effects, the airfoils are discussed in the order presented in Fig. 3 (alphabetically).

It should also be stated from the outset that each airfoil presented here was designed with unique and different constraints and desired performance characteristics in mind. Consequently, the airfoils collectively represent a broad range of performance characteristics and geometric properties. Hence, to compare directly the performance of one airfoil to the next and declare one airfoil better than another would be misleading. Therefore, again, the focus will be on highlighting interesting and important performance characteristics while leaving design decisions and the es-
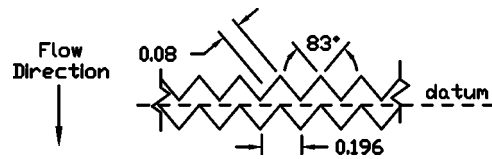
Fig. 14 Boundary layer trip geometry used to simulate the effects of leading edge debris and errosion (dimensions are in inches)

tablishment of various figures of merit to the wind turbine blade designer whose task goes beyond the scope of topics discussed here.

Finally, to simulate the effects of roughness caused by leading-edge debris and erosion, the airfoils were tested with three-dimensional zigzag boundary-layer trips afixed to the upper and lower surfaces near the leading edge. In particular, the trips were 0.013 in. high (0.11% of chord), and they were located on the upper and lower surfaces at 2% and 5% of chord, respectively. These data are discussed along with the "clean" airfoil data, that is, data taken on the airfoils without boundary layer trips. Figure 14 shows a drawing of the boundary-layer trip used in this study. It is denoted as "zigzag trip type F" because it is the sixth different zigzag trip geometry tested at UIUC.

E387. The E387 airfoil was designed in the early 1960s by Richard Eppler for use on model sailplanes. It was quickly successful and is still used for that application. Beyond this, it has taken on the additional role of becoming a benchmark section used to compare low Reynolds number airfoil measurements from one wind tunnel facility with another. In fact, the E387 airfoil is likely the most widely tested low Reynolds number section having been tested at Delft in the Netherlands, Stuttgart, Princeton, NASA Langley and UIUC prior to and including the current tests. Having already discussed the comparison between the UIUC data and that of NASA Langley, the focus in this section is on elucidating the low Reynolds number performance characteristics.

Figures 15 and 16 show the drag polars and the lift and drag characteristics at Reynolds numbers of 100,000, 200,000, 300,000, 350,000, 460,000, and 500,000. [The Re=460,000 case was added for comparison with Langley.] For the lowest Reynolds number of 100,000, the most prominent manifestation of a laminar separation bubble is observed in the drag polar. Between the limits of the low drag range, there is an increase in drag associated principally with a laminar separation bubble. In the vicinity of corners of the low drag range, the laminar separation bubble is short or nonexistent and the drag is not as high. However, as the angle of attack is increased from the lower corner, the adverse pressure gradient on the upper surface becomes stronger and as a result the bubble drag grows until the drag is a maximum near a lift coefficient of 0.7 ($\alpha \approx 3$ deg). Beyond this point, the size of the bubble begins to decrease (see Fig. 21 of Ref. [12]), which results in lower drag until the upper corner of the polar is reached (lift coefficient of 1.1). Here transition takes place on the surface without a drag producing bubble being present. As the Reynolds number increases, the advantages of higher Reynolds number and a reduction in the length of the bubble (due to earlier transition, see Fig. 8) leads to correspondingly lower drag.

As mentioned, for all airfoils, a zigzag boundary layer trip was added on the top and bottom surfaces near the leading edge to simulate the effects of roughness caused by debris and erosion that occurs on wind turbine blades over time. In general, the main effect of the trip is to promote transition shortly downstream of the trip. If a bubble is present in the clean case, the trip has the effect of shortening the laminar separation bubble. When there is no bubble, transition is forced to occur sooner than it otherwise would.

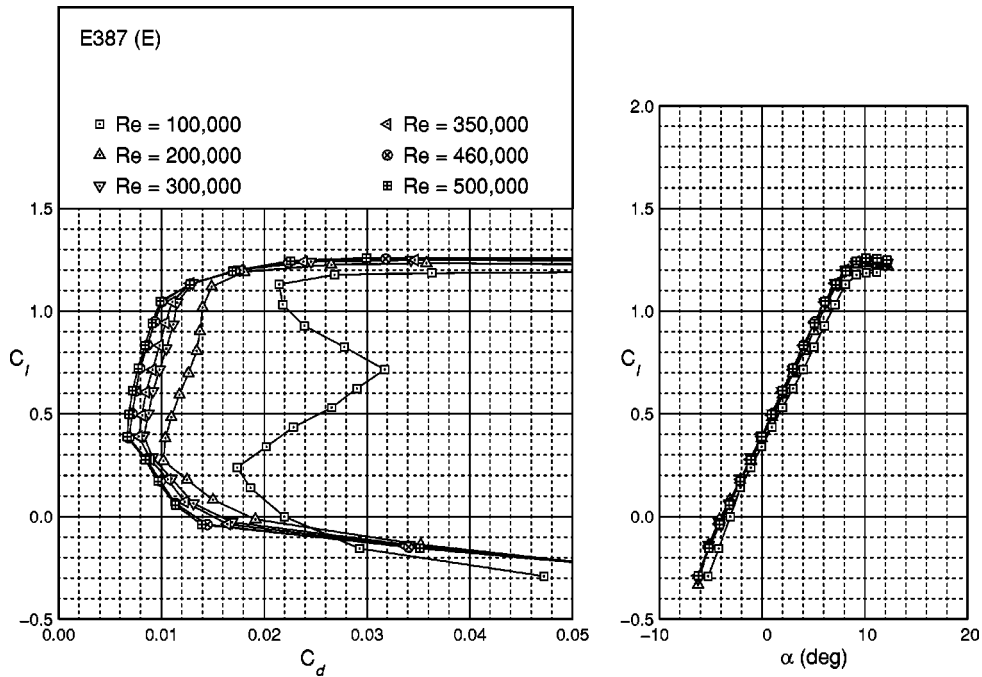In terms of performance, the beneficial effect of shortening the

Fig. 15   Drag polar for the E387 (E)

bubble (and hence lowering the drag) is, to some degree, offset by the increased length of turbulent flow. The net effect can be either beneficial (when the bubble is otherwise large) or a hinderence (when the bubble is small or not present at all). As a result, the performance with boundary layer trips used at low Reynolds numbers is often complex.

For the E387, the effects of the trip are clearly seen when comparing the drag polars shown in Fig. 15 to those in Fig. 16. For Re=100,000, the drag is overall reduced due to the shortened laminar separation bubble. In the middle of the polar, the kink

where the drag begins to reduce with increasing angle of attack occurs at a lower lift coefficient ($C_l \approx 0.55$) due to transition being promoted by the boundary layer trip in addition to the pressure gradient effect that is beneficial in both the clean and tripped cases.

The effects of the trip are also apparent in the lift curves. [4] For the clean case at Re=100,000, the life curve is offset slightly below the curves for the higher Reynolds numbers. This offset is caused by a decambering effect that results from the added displacement thickness produced by the large bubble. When the
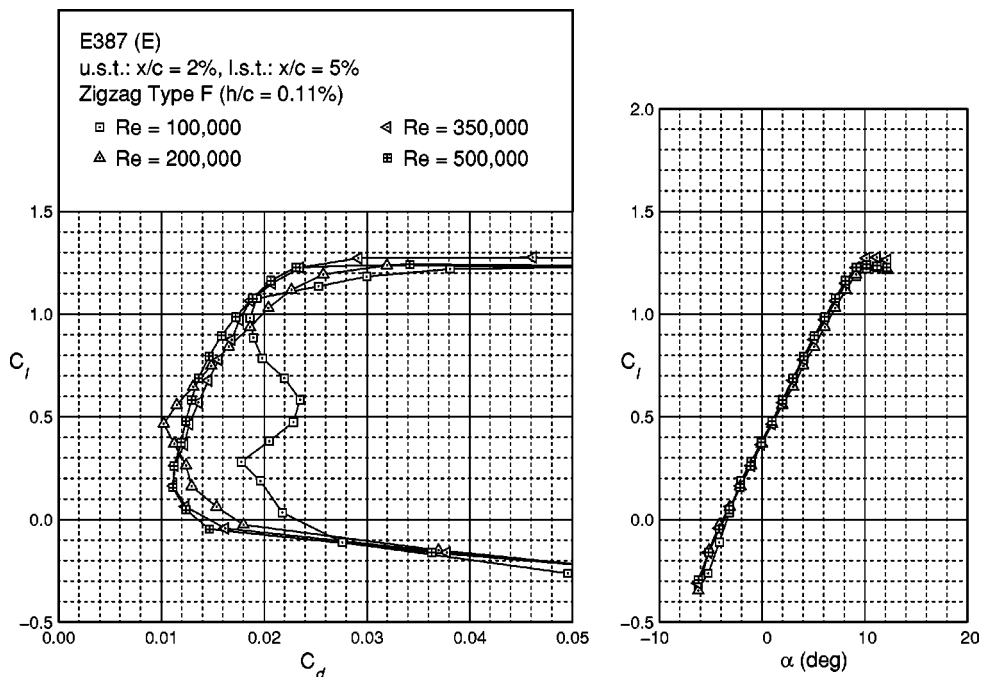

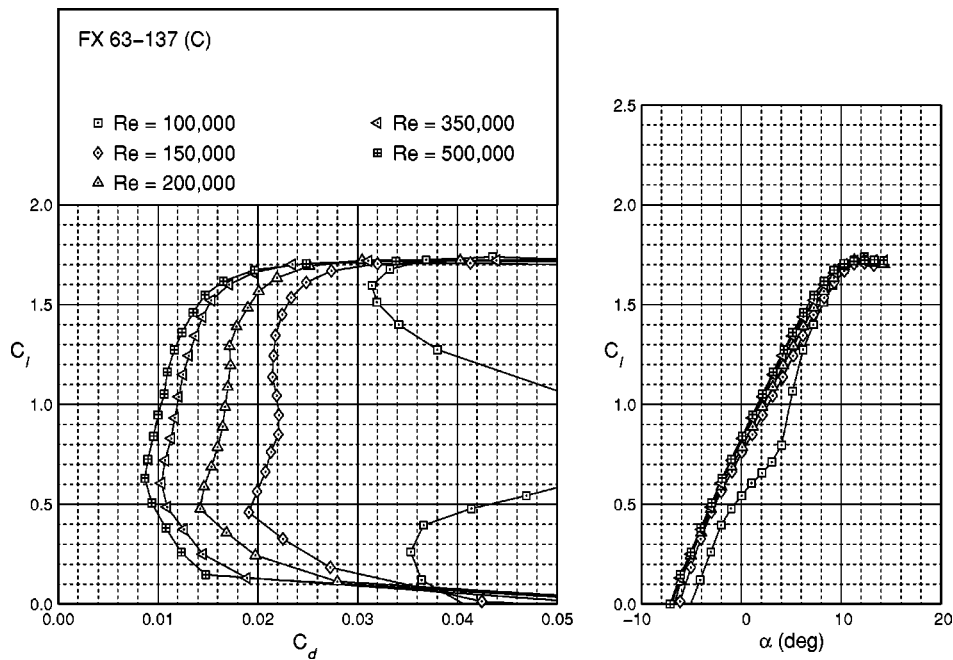**Fig. 16   Drag polar for the E387 (E) with trip type F**

Fig. 17 Drag polar for the FX 63-137 (C)

bubble is reduced in size by using a trip, this displacement thickness effect is smaller, and the lift curve for Re=100,000 nearly coincides with the higher Reynolds number cases that have smaller bubbles.

For Re=200,000 with the boundary layer trip, only at a lift coefficient of ≈ 0.47 is the drag lower than the clean case. Thus, for this condition, the tradeoff between having lower bubble drag and higher turbulent skin friction drag leads to lower net drag, while for all other points the added turbulent skin friction drag outweighs the reduction in the bubble drag, resulting in higher drag with the trip. This tradeoff, leading to higher drag, is particularly true for the higher Reynolds number cases.

Finally, from the lift curves presented in Ref. [4], it is interesting to note that there is a negligible drop in the maximum lift coefficient due to roughness effects for this airfoil. This results from transition occurring very near the leading edge for all angles of attack below the airfoil maximum lift coefficient. Thus, at maximum lift the flow on the upper surface for the most part behaves the same whether or not there is a trip, and hence the stall performance has little dependence on the presence of the trip. This general understanding of the connection between the airfoil maximum lift and transition, which is discussed in Ref. [18], can be used to provide insight into the case of a leading edge separation bubble at stall, which is what happens at low Reynolds numbers. In such a case, the boundary layer trip can be completely or partially immersed in the recirculating zone of the bubble. When this occurs, the airfoil stall can be quite insensitive to a discrete roughness element such as the type tested in this study.

FX 63-137. This airfoil was designed by F.X. Wortmann for the Liver Puffin human-powered aircraft. It has since been used for many low Reynolds number applications due to its high-lift, soft-stall characteristics and overall good performance. In particular, in the small wind turbine arena, it has been used by Aeromag (Lakota wind turbine) and Southwest Windpower (H-40 and H-80 wind turbines) and the now defunct Worldpower Technologies.

The original coordinates for this section as well as several other early Wortmann sections [19], are not analytically smooth presumably due to a small numerical error in the design method. As described in Ref. [20] (which includes computational performance predictions on the six airfoils in this study), the original coordinates were smoothed for use in computations, and those coordinates have been used in this experimental study.

As deduced from the high camber, this airfoil should be expected to produce considerably more lift than the E387. Indeed, as shown in Fig. 17, the FX 63-137 produces a $C_{l,\max}$ of approximately 1.7. However, for Re=100,000, the airfoil suffers the consequences of a large laminar separation bubble. In fact, at the lower angles of attack, it is likely that the bubble does not close on the airfoil, but instead extends into the wake. Two observations support this conclusion. First, the lift curve at Re=100,000 for low angles of attack falls considerably below the curves for higher Reynolds numbers. Second, for the same low Reynolds number condition, the drag is quite high. At an angle of attack of approximately 4°, the situation improves as the bubble begins to attach to the airfoil. The lift increases and the drag is correspondingly reduced.

This airfoil, along with the S822 and S834, was tested at an intermediate Reynolds number of 150,000 to obtain more resolution in the low Reynolds number range where the drag changes dramatically. As seen in Fig. 17, a large drag reduction is observed for the Re=150,000 case. Concurrent with this, the large offset in the lift curve is absent. Both of these observations indicate a reduction in the size of the laminar separation bubble versus the Re=100,000 case. As would be expected the performance continues to improve with higher Reynolds number.

When boundary layer trips are applied, the performance follows trends similar to those described for the E387. First, for Re=100,000, the effects of the bubble are mitigated as seen by the slight rise in the lift curve and by the reduction in drag. For the higher Reynolds numbers, the polars tend to collapse onto an envelope, which implies that the flow on the upper surface experiences early transition (before the airfoil reaches maximum lift coefficient) and the absence of a laminar separation bubble. For points that fall on either side of this envelope, a bubble still exists.

In the polars, there is an interesting trend reversal where the drag first decreases and then increases as the Reynolds number is increased for a fixed angle of attack. One instance of this is seen for an angle of attack of 4 deg, corresponding to a lift coefficient
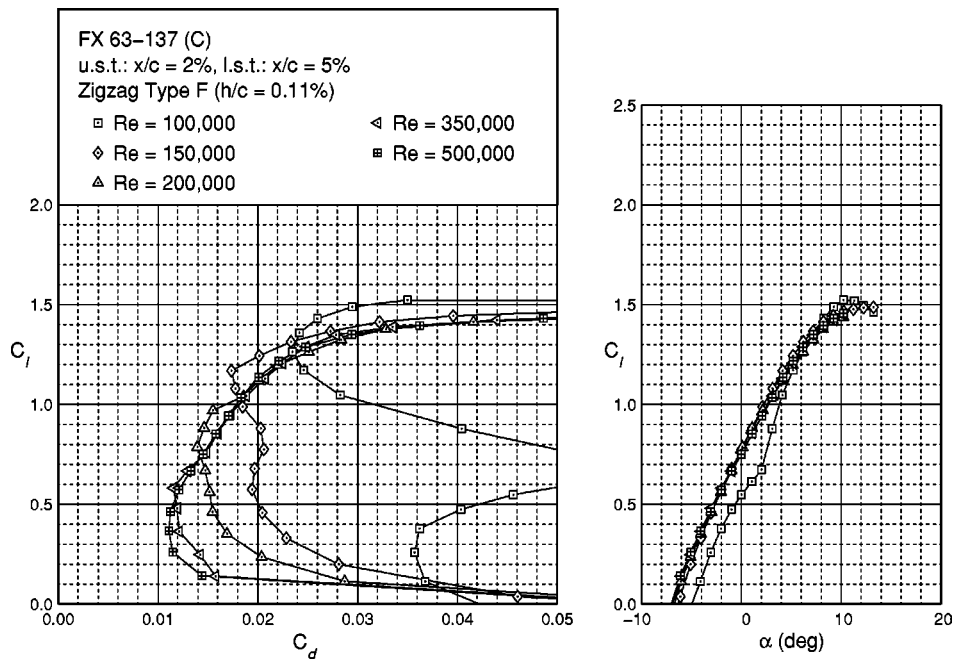
Fig. 18   Drag polar for the FX 63-137 (C) with trip type F

of approximately 0.7. This same type of behavior was seen for the E387 at an angle of attack of 1 deg ($C_l \approx 0.47$). As previously described, there is first a drag reduction due to a shortening of the bubble and then a drag rise due to the added turbulent flow as the Reynolds number is increased. This same behavior can be identified in the performance of all of the tripped airfoil polars.

Other items to note include the following. Unlike the E387 airfoil, the maximum lift performance of the FX 63-137 suffers from the addition of simulated roughness. Overall the drop in

$C_{l,max}$ is 0.2. Another difference is that while the E387 had a highly unsteady stall leading to a sharp break, the FX 63-137 exhibited a soft stall with little unsteadiness (Fig. 18).

S822 and S834.   As described in Ref. [20], the S822 and S834 were both developed by NREL for use on small wind turbines and are now available under license. The S822 airfoil has been used on the AOC/Windlite and Havatex [21] small wind turbines. Briefly, the S822 and S834 were designed for the outer blade span
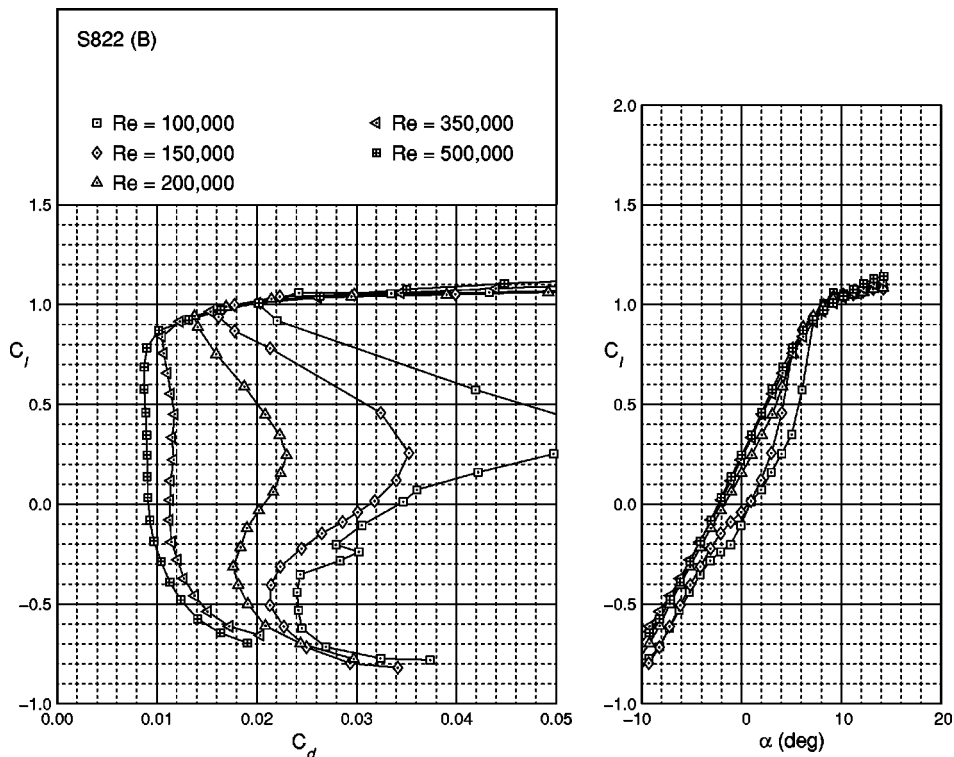

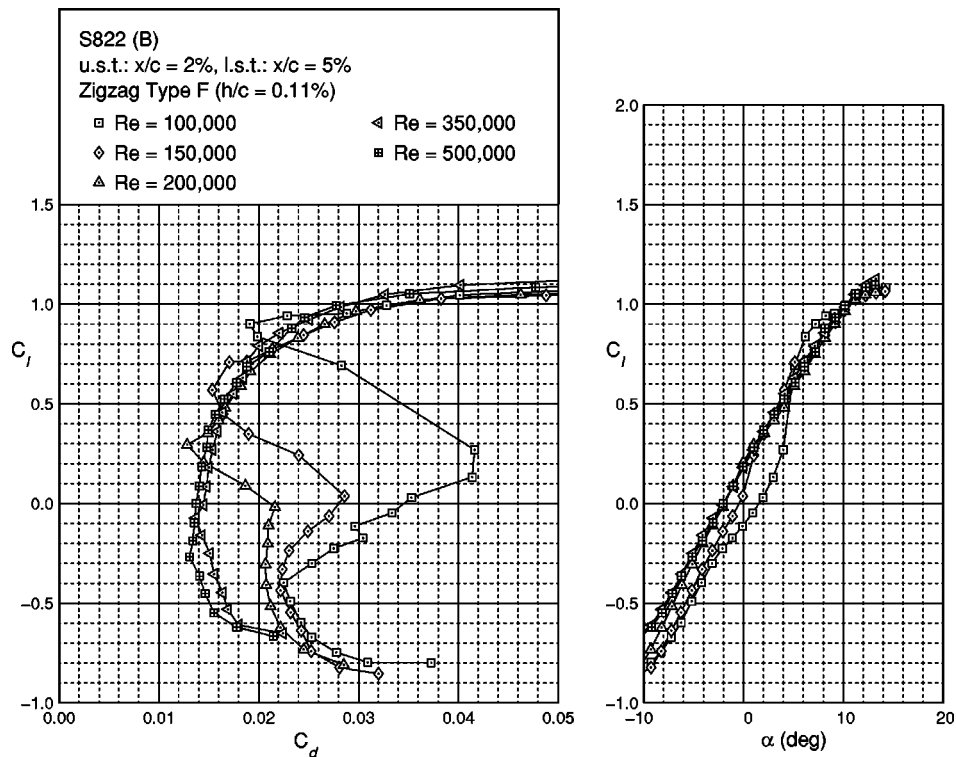**Fig. 19   Drag polar for the S822 (B)**

Fig. 20 Drag polar for the S822 (B) with trip type F

of rotors having diameters in the range 3–10 and 1–3 m, respectively. The newer S834 was designed for low-noise, which was not a consideration in the design of the S822 section.

The performance of these airfoils is shown in Figs. 19–22. Many of the general characteristics previously described are exhibited by these two airfoils. Differences in the details are, of

course, dictated by the associated design goals that collectively lead to the resulting performance discussed below.

For both airfoils, the often characteristic high-drag knee in the drag polar at the lower Reynolds numbers due to the presence of a laminar separation is observed. The associated nonlinearities (offsets) in the lift curves are also seen for Re=100,000 and
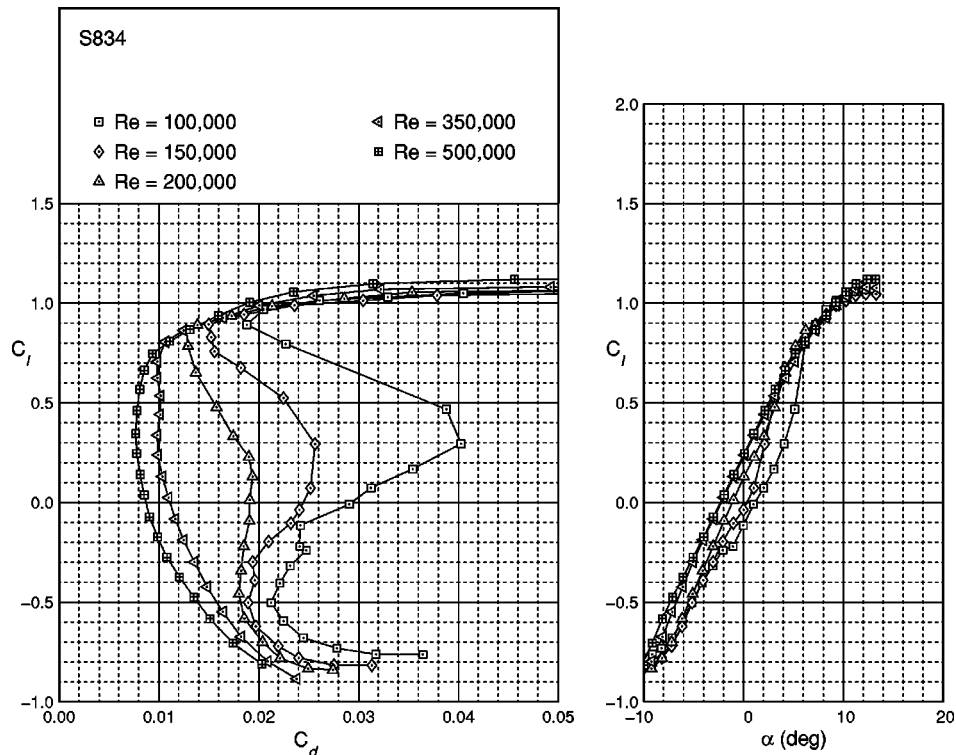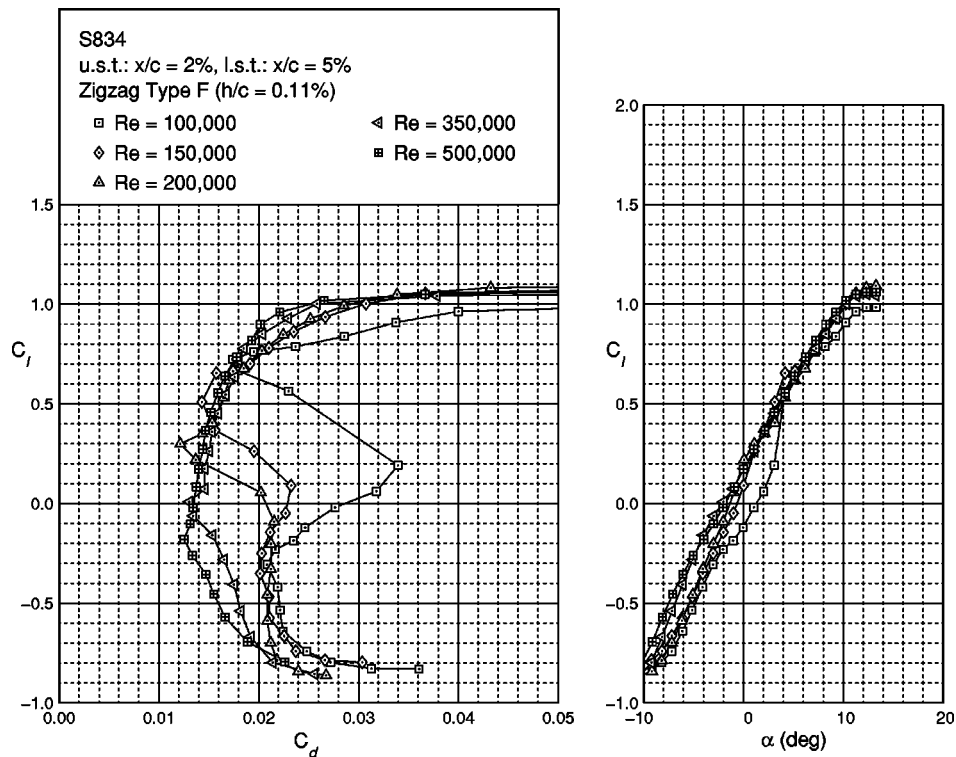

Fig. 21 Drag polar for the S834

Fig. 22 Drag polar for the S834 with trip type F

150,000 and, to a slight extent, for Re=200,000. This behavior is also reflected in the drag polars, where the high-drag knee is more exaggerated than that for the FX 63-137.

Adding the zigzag boundary layer trips to both airfoils yields lower drag at the lower Reynolds numbers, as would be expected from the past cases examined. Also, as would be expected, the nonlinearities seen in the lift curves are mitigated somewhat by the boundary layer trips. However, the boundary layer trip on the upper surface is not large enough to completely eliminate the

bubble for Re=100,000. This is shown by the 2 deg range in the middle of the polar where the lift increases nonlinearly ($\Delta C_l \approx 0.5$) for both airfoils.

The S834, being designed for smaller rotors, was designed for lower Reynolds numbers. This trend is apparent in the drag polars where it is observed that the S834 has better performance than the S822 at low Reynolds numbers. The differences are mostly slight as one might expect from the similarities in the geometries and pressure distributions [4].
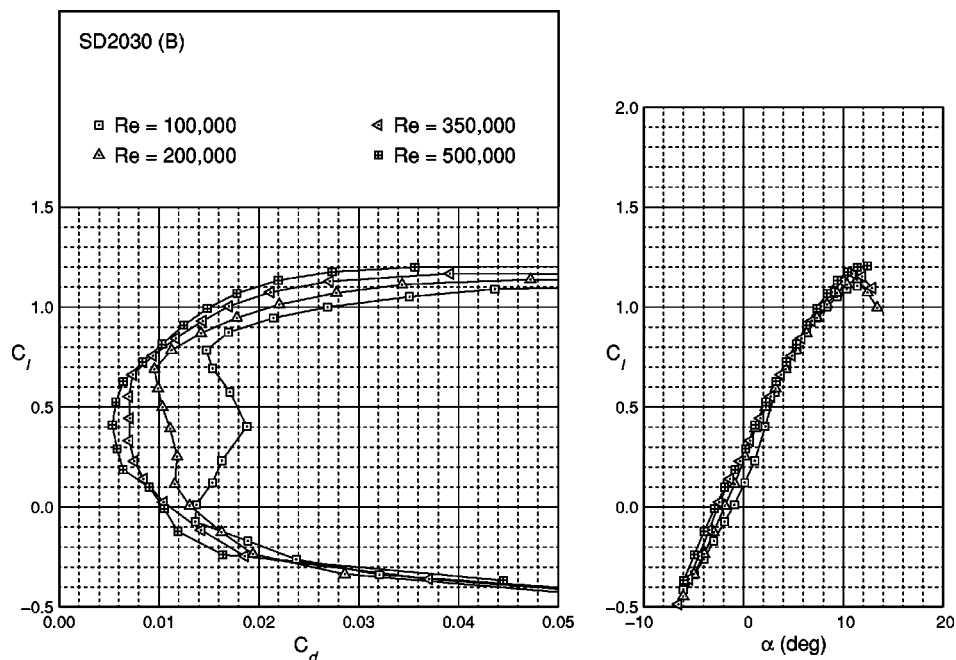

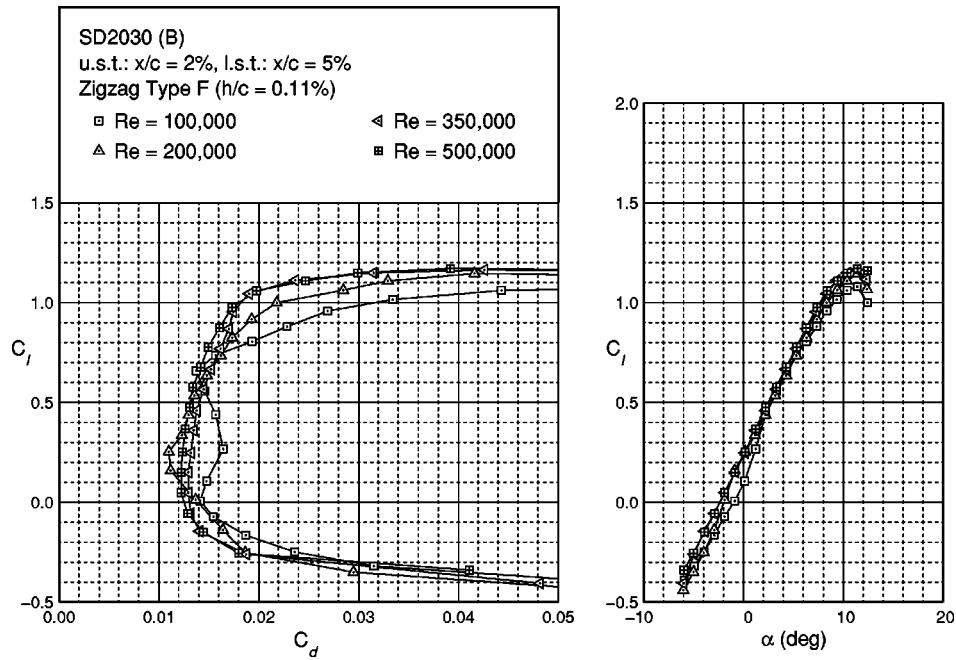Fig. 23 Drag polar for the SD2030 (B)

Fig. 24 Drag polar for the SD2030 (B) with trip type F

For both airfoils, unsteadiness at stall prevented taking high angle of attack data for Re=500,000. The degree of the unsteadiness during the tests was observed to be somewhat less than that for the E387.

SD2030. This Selig/Donovan airfoil presented in Ref. [17] was originally designed for model sailplanes. It has since been used on the Southwest Windpower Air 403 and Air X small wind turbines. Figures 23 and 24 show the performance characteristics.

As compared with the other airfoils discussed, this airfoil has quite low drag at the expense of a narrower drag polar. A high-drag knee is present for Re=100,000; however, the peak drag at the kink is much lower than that seen for the other airfoils tested. This low drag is achieved by having a long transition ramp, or "bubble ramp [17]," that leads to a thin laminar separation bubble. The causes for other general effects seen in the figures have been previously explained.
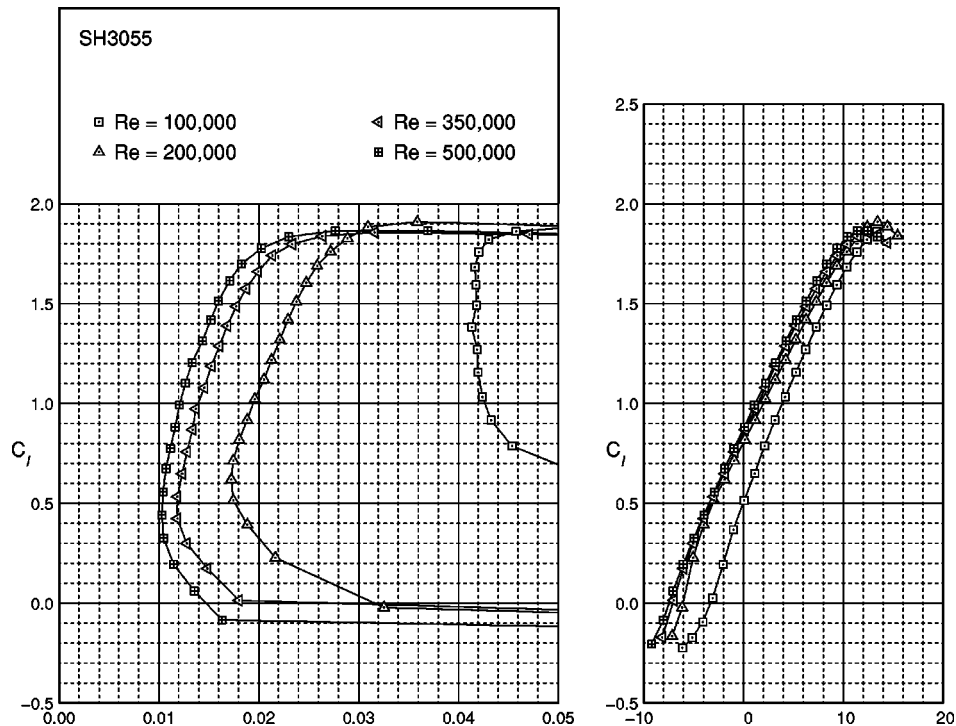

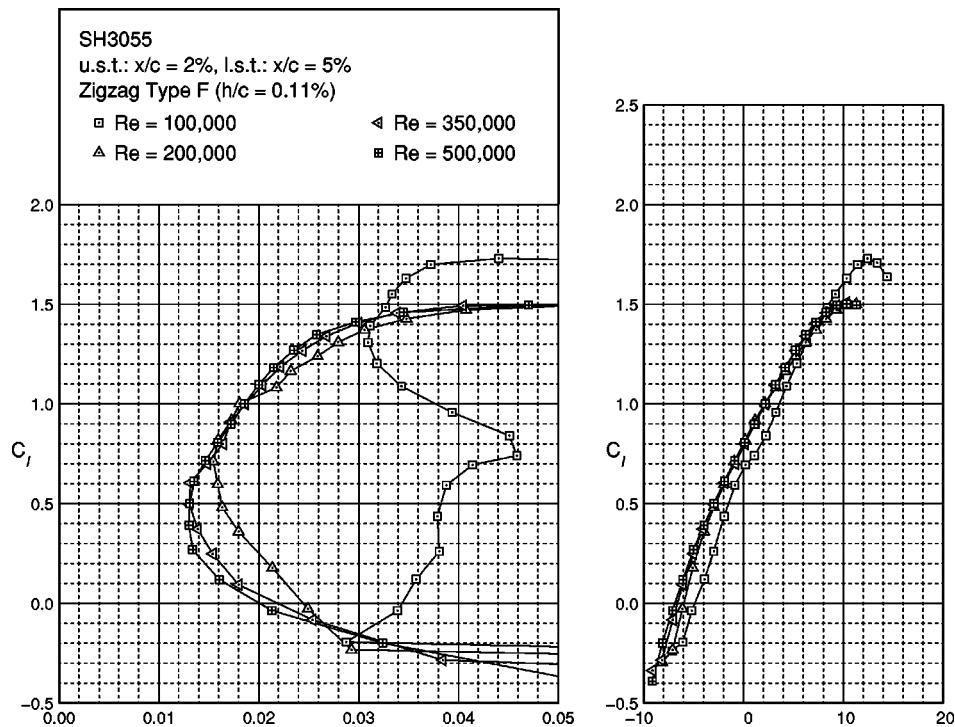**Fig. 25 Drag polar for the SH3055**

Fig. 26 Drag polar for the SH3055 with trip type F

Of the six airfoils tested, this airfoil displayed the most unsteadiness in stall, and this limited the angle of attack range for the Re=500,000 case.

SH3055. The Selig/Hanley airfoil (see Figs. 25 and 26), derived from prior SH/Bergey designs, is intended for a 7-m diameter variable-speed wind turbine to be manufactured by Bergey WindPower Co. For the lowest Reynolds number case (Re =100,000), there is a considerable drop in lift as compared with the higher Reynolds number cases. This drop and associated high drag is likely caused by a laminar separation bubble that does not reattach to the airfoil over the majority of the lift range. Moreover, at the lowest angles of attack tested, it is speculated that the lower surface of the airfoil is stalled as well, which further decambers the section. For the higher Reynolds numbers, the performance improves as was seen with past examples. Boundary layer trips applied to the airfoil lead to improved performance for Re =100,000, but at higher Reynolds numbers the performance is mostly handicapped as has been observed with the other sections. Finally, for this airfoil, the stall behavior was quite gentle.

It should be mentioned that for all of the airfoils the comments regarding the degree of the unsteadiness in stall are qualitative. Quantitative data on the unsteady stalling of airfoils at low Reynolds numbers can be found Ref. [22]. In that study, it was concluded that airfoils that exhibited a thin-airfoil stall, such as the E387, were quite susceptible to large fluctuations in lift while a trailing edge stall led to small fluctuations.

Summary

An extensive database of performance characteristics on several low Reynolds number airfoils applicable to small wind turbines has been documented and discussed. Prior to the collection of these data, an extensive wind tunnel flow quality study was performed to validate the test environment. Moreover, the data acquisition and reduction procedures were validated by comparing UIUC data on the E387 airfoil with that taken at NASA Langley. These data compliment a companion study that focused on the aeroacoustics of these airfoils. Collectively the performance data presented in this paper and the related aeroacoustic data should aid designers in balancing the tradeoffs between rotor noise and performance.

Acknowledgments

References

[1] Oerlemans, S., and Migliore, P., 2004, "Wind Tunnel Aeroacoustic Tests on Six Airfoils for Use on Small Wind Turbines," NREL/SR-500-34470.
[2] Selig, M. S., Guglielmo, J. J., Broeren, A. P., and Giguère, P., 1995, *Summary of Low-Speed Airfoil Data*, SoarTech, Virginia Beach, VA, Vol. 1.
[3] Lyon, C. A., Broeren, A. P., Giguère, P., Gopalarathnam, A., and Selig, M. S., 1998, *Summary of Low-Speed Airfoil Data*, SoarTech, Virginia Beach, VA, Vol. 3.
[4] McGranahan, B. D., and Selig, M. S., 2004, "Wind Tunnel Aerodynamic Tests on Six Airfoils for Use on Small Wind Turbines," NREL/SR-500-34515.
[5] Guglielmo, J. J., and Selig, M. S., 1996, "Spanwise Variations in Profile Drag for Airfoils at Low Reynolds Numbers," J. Aircraft, **33**, pp. 699–707.
[6] McGhee, R. J., Walker, B. S., and Millard, B. F., 1988, "Experimental Results for the Eppler 387 Airfoil at Low Reynolds Numbers in the Langley Low-Turbulence Pressure Tunnel," NASA TM-4062.
[7] Rae, W. H., Jr., and Pope, A., 1984, *Low-Speed Wind Tunnel Testing*, Wiley, New York. ISBN 0-471-87402-7.
[8] Bragg, M. B., and Lu, B., 2000, "Experimental Investigation of Airfoil Drag Measurement With Simulated Leading-Edge Ice Using the Wake Survey Method," AIAA Pap. 2000-3919.
[9] Evangelista, R., McGhee, R. J., and Walker, B. S., 1989, "Correlation of Theory to Wind-Tunnel Data at Reynolds Numbers Below 500,000," *Low*

Reynolds Number Aerodynamics, edited by T. J. Mueller, Lecture Notes in Engineering, Vol. 54, Springer, New York, pp. 131–145. ISBN 3-540-51884-3.

[10] Briley, R. W., and McDonald, H., 1975, ''Numerical Prediction of Incompressible Separation Bubbles,'' J. Fluid Mech., **69**, pp. 631–656.

[11] Kwon, O. K., and Pletcher, R. H., 1919, ''Prediction of Incompressible Separated Boundary Layers Including Viscous-Inviscid Interaction,'' Trans ASME, **101**, pp. 466–472.

[12] Davis, R. L., and Carter, J. E., 1984, ''Analysis of Airfoil Transitional Separation Bubbles,'' NASA CR-3791.

[13] Walker, G. J., Subroto, P. H., and Platzer, M. F., 1988, ''Transition Modeling Effects on Viscous/Inviscid Interaction Analysis of Low Reynolds Number Airfoil Flows Involving Laminar Separation Bubbles,'' ASME Paper, 88-GT-32.

[14] Huebsch, W. W., and Rothmayer, A. P., 1998, ''The Effects of Small-Scale Surface Roughness on Laminar Airfoil-Scale Trailing Edge Separation Bubbles,'' AIAA Pap. 98-0103.

[15] Alam, M., and Sandham, N. D., 2000, ''Direct Numerical Simulation of 'Short' Laminar Separation Bubbles With Turbulent Reattachment,'' J. Fluid Mech., **403**, pp. 223–250.

[16] Lin, J. C. M., and Pauley, L. L., 1996, ''Low-Reynolds-Number Separation on an Airfoil,'' AIAA J., **34**, pp. 1570–1577.

[17] Selig, M. S., Donovan, J. F., and Fraser, D. B., 1989, *Airfoils at Low Speeds*, Soartech 8, SoarTech, Virginia Beach, VA.

[18] Somers, D. M., 1992, ''Subsonic Natural-Laminar-Flow Airfoils,'' *Natural Laminar Flow and Laminar Flow Control*, edited by R. W. Barnwell and M. Y. Hussaini, Springer, New York, pp. 143–176.

[19] Althaus, D., and Wortmann, F. X., 1981, *Stuttgarter Profilkatalog I*, Friedr. Vieweg & Sohn, Braunschweig/Weisbaden.

[20] Somers, D. M., and Maughmer, M. D., 2003, ''Theoretical Aerodynamic Analyses of Six Air-Foils for Use on Small Wind Turbines,'' NREL/SR-500-33295.

[21] Vick, B. D., and Clark, R. N., 2000, ''Testing of a 2-Kilowatt Wind-Electric System for Water Pumping,'' WINDPOWER, Palm Springs, CA.

[22] Broeren, A. P., and Bragg, M. B., 2001, ''Unsteady Stalling Characteristics of Thin Airfoils at Low Reynolds Numbers,'' *Fixed and Flapping Wing Aerodynamics for Micro Air Vehicle Applications*, edited by T. J. Mueller, Progress in Astronautics and Aeronautics Vol. 195, AIAA, New York, pp. 191–213.